

Two-particle correlations on transverse momentum and momentum dissipation in Au–Au collisions at $\sqrt{s_{NN}} = 130$ GeV

The STAR Collaboration

J Adams¹, M M Aggarwal², Z Ahammed³, J Amonett⁴, B D Anderson⁴, M Anderson⁵, D Arkhipkin⁶, G S Averichev⁷, Y Bai⁸, J Balewski⁹, O Barannikova¹, L S Barnby¹, J Baudot¹⁰, S Bekele¹¹, V V Belaga⁷, A Bellingeri-Laurikainen¹², R Bellwied¹³, B I Bezverkhny¹⁴, S Bhardwaj¹⁵, A Bhasin¹⁶, A K Bhati², H Bichsel¹⁷, J Bielcik¹⁴, J Bielcikova¹⁴, L C Bland¹⁸, C O Blyth¹, S-L Blyth¹⁹, B E Bonner²⁰, M Botje⁸, J Bouchet¹², A V Brandin²¹, A Bravar¹⁸, M Bystersky²², R V Cadman²³, X Z Cai²⁴, H Caines¹⁴, M Calderón de la Barca Sánchez⁶, J Castillo⁸, O Catu¹⁴, D Cebra⁵, Z Chajecki¹¹, P Chaloupka²², S Chattopadhyay³, H F Chen²⁵, J H Chen²⁴, Y Chen²⁶, J Cheng²⁷, M Cherney²⁸, A Chikhanian¹⁴, H A Choi²⁹, W Christie¹⁸, J P Coffin¹⁰, T M Cormier¹³, M R Cosentino³⁰, J G Cramer¹⁷, H J Crawford³¹, D Das³, S Das³, M Daugherty³², M M de Moura³⁰, T G Dedovich⁷, M DePhillips¹⁸, A A Derevschikov³³, L Didenko¹⁸, T Dietel³⁴, P Djawotho⁹, S M Dogra¹⁶, W J Dong²⁶, X Dong²⁵, J E Draper⁵, F Du¹⁴, V B Dunin⁷, J C Dunlop¹⁸, M R Dutta Mazumdar³, V Eckardt³⁵, W R Edwards¹⁹, L G Efimov⁷, V Emelianov²¹, J Engelage³¹, G Eppley²⁰, B Erasmus¹², M Estienne¹⁰, P Fachini¹⁸, R Fatemi³⁶, J Fedorisin⁷, K Filimonov¹⁹, P Filip⁶, E Finch¹⁴, V Fine¹⁸, Y Fisyak¹⁸, J Fu³⁷, C A Gagliardi³⁸, L Gaillard¹, J Gans¹⁴, M S Ganti³, V Ghazikhanian²⁶, P Ghosh³, J E Gonzalez²⁶, Y G Gorbunov²⁸, H Gos³⁹, O Grebenyuk⁸, D Grosnick⁴⁰, S M Guertin²⁶, K S F F Guimaraes³⁰, Y Guo¹³, N Gupta¹⁶, T D Gutierrez⁵, B Haag⁵, T J Hallman¹⁸, A Hamed¹³, J W Harris¹⁴, W He⁹, M Heinz¹⁴, T W Henry³⁸, S Hepplemann⁴¹, B Hippolyte¹⁰, A Hirsch⁴², E Hjort¹⁹, G W Hoffmann³², M J Horner¹⁹, H Z Huang²⁶, S L Huang²⁵, E W Hughes⁴³, T J Humanic¹¹, G Igo²⁶, A Ishihara³², P Jacobs¹⁹, W W Jacobs⁹, P Jakl²², F Jia⁴⁴, H Jiang²⁶, P G Jones¹, E G Judd³¹, S Kabana¹², K Kang²⁷, J Kapitan²², M Kaplan⁴⁵, D Keane⁴, A Kechechyan⁷, V Yu Khodyrev³³, B C Kim²⁹, J Kiryluk³⁶, A Kisiel³⁹, E M Kislov⁷, S R Klein¹⁹, D D Koetke⁴⁰, T Kollegger³⁴, M Kopytine⁴, L Kotchenda²¹, V Kouchpil²², K L Kowalik¹⁹, M Kramer⁴⁶, P Kravtsov²¹, V I Kravtsov³³, K Krueger²³, C Kuhn¹⁰, A I Kulikov⁷, A Kumar², A A Kuznetsov⁷, M A C Lamont¹⁴, J M Landgraf¹⁸, S Lange³⁴, S LaPointe¹³, F Laue¹⁸, J Lauret¹⁸, A Lebedev¹⁸, R Lednicky⁶, C-H Lee²⁹, S Lehocka⁷, M J LeVine¹⁸, C Li²⁵, Q Li¹³, Y Li²⁷, G Lin¹⁴, S J Lindenbaum⁴⁶, M A Lisa¹¹, F Liu³⁷, H Liu²⁵, J Liu²⁰, L Liu³⁷, Z Liu³⁷, T Ljubicic¹⁸, W J Llope²⁰, H Long²⁶, R S Longacre¹⁸, M Lopez-Noriega¹¹,

W A Love¹⁸, Y Lu³⁷, T Ludlam¹⁸, D Lynn¹⁸, G L Ma²⁴, J G Ma²⁶,
 Y G Ma²⁴, D Magestro¹¹, D P Mahapatra⁴⁷, R Majka¹⁴, L K Mangotra¹⁶,
 R Manweiler⁴⁰, S Margetis⁴, C Markert⁴, L Martin¹², H S Matis¹⁹,
 Yu A Matulenko³³, C J McClain²³, T S McShane²⁸, Yu Melnick³³,
 A Meschanin³³, M L Miller³⁶, N G Minaev³³, S Mioduszewski³⁸,
 C Mironov⁴, A Mischke⁸, D K Mishra⁴⁷, J Mitchell²⁰, B Mohanty³,
 L Molnar⁴², C F Moore³², D A Morozov³³, M G Munhoz³⁰, B K Nandi⁴⁸,
 C Nattrass¹⁴, T K Nayak³, J M Nelson¹, P K Netrakanti³, V A Nikitin⁶,
 L V Nogach³³, S B Nurushev³³, G Odyniec¹⁹, A Ogawa¹⁸, V Okorokov²¹,
 M Oldenburg¹⁹, D Olson¹⁹, M Pachr²², S K Pal³, Y Panebratsev⁷,
 S Y Panitkin¹⁸, A I Pavlinov¹³, T Pawlak³⁹, T Peitzmann⁸,
 V Perevoztchikov¹⁸, C Perkins³¹, W Peryt³⁹, V A Petrov¹³, S C Phatak⁴⁷,
 R Picha⁵, M Planinic⁴⁹, J Pluta³⁹, N Poljak⁴⁹, N Porile⁴², J Porter¹⁷,
 A M Poskanzer¹⁹, M Potekhin¹⁸, E Potrebenikova⁷, B V K S Potukuchi¹⁶,
 D Prindle¹⁷, C Pruneau¹³, J Putschke¹⁹, G Rakness⁴¹, R Raniwala¹⁵,
 S Raniwala¹⁵, R L Ray³², S V Razin⁷, J G Reid¹⁷, J Reinnarth¹²,
 D Relyea⁴³, F Retiere¹⁹, A Ridiger²¹, H G Ritter¹⁹, J B Roberts²⁰,
 O V Rogachevskiy⁷, J L Romero⁵, A Rose¹⁹, C Roy¹², L Ruan¹⁹,
 M J Russcher⁸, R Sahoo⁴⁷, I Sakrejda¹⁹, S Salur¹⁴, J Sandweiss¹⁴,
 M Sarsour³⁸, P S Sazhin⁷, J Schambach³², R P Scharenberg⁴²,
 N Schmitz³⁵, K Schweda¹⁹, J Seger²⁸, I Selyuzhenkov¹³, P Seyboth³⁵,
 A Shabetai¹⁹, E Shahaliev⁷, M Shao²⁵, M Sharma², W Q Shen²⁴,
 S S Shimanskiy⁷, E Sichtermann¹⁹, F Simon³⁶, R N Singaraju³,
 N Smirnov¹⁴, R Snellings⁸, G Sood⁴⁰, P Sorensen¹⁸, J Sowinski⁹, J Speltz¹⁰,
 H M Spinka²³, B Srivastava⁴², A Stadnik⁷, T D S Stanislaus⁴⁰, R Stock³⁴,
 A Stolpovsky¹³, M Strikhanov²¹, B Stringfellow⁴², A A P Suaide³⁰,
 E Sugarbaker¹¹, M Sumbera²², Z Sun⁴⁴, B Surrow³⁶, M Swanger²⁸,
 T J M Symons¹⁹, A Szanto de Toledo³⁰, A Tai²⁶, J Takahashi³⁰,
 A H Tang¹⁸, T Tarnowsky⁴², D Thein²⁶, J H Thomas¹⁹, A R Timmins¹,
 S Timoshenko²¹, M Tokarev⁷, T A Trainor¹⁷, S Trentalange²⁶,
 R E Tribble³⁸, O D Tsai²⁶, J Ulery⁴², T Ullrich¹⁸, D G Underwood²³,
 G Van Buren¹⁸, N van der Kolk⁸, M van Leeuwen¹⁹, A M Vander
 Molen⁵⁰, R Varma⁴⁸, I M Vasilevski⁶, A N Vasiliev³³, R Vernet¹⁰,
 S E Vigdor⁹, Y P Viyogi³, S Vokal⁷, S A Voloshin¹³, W T Waggoner²⁸,
 F Wang⁴², G Wang²⁶, J S Wang⁴⁴, X L Wang²⁵, Y Wang²⁷, J W Watson⁴,
 J C Webb⁴⁰, G D Westfall⁵⁰, A Wetzler¹⁹, C Whitten Jr²⁶, H Wieman¹⁹,
 S W Wissink⁹, R Witt¹⁴, J Wood²⁶, J Wu²⁵, N Xu¹⁹, Q H Xu¹⁹, Z Xu¹⁸,
 P Yepes²⁰, I-K Yoo²⁹, V I Yurevich⁷, W Zhan⁴⁴, H Zhang¹⁸, W M Zhang⁴,
 Y Zhang²⁵, Z P Zhang²⁵, Y Zhao²⁵, C Zhong²⁴, R Zoukarneev⁶,
 Y Zoukarneeva⁶, A N Zubarev⁷ and J X Zuo²⁴

¹ University of Birmingham, Birmingham, UK

² Panjab University, Chandigarh 160 014, India

³ Variable Energy Cyclotron Centre, Kolkata 700 064, India

⁴ Kent State University, Kent, OH 44242, USA

⁵ University of California, Davis, CA 95616, USA

⁶ Particle Physics Laboratory (JINR), Dubna, Russia

⁷ Laboratory for High Energy (JINR), Dubna, Russia

⁸ NIKHEF and Utrecht University, Amsterdam, The Netherlands

⁹ Indiana University, Bloomington, IN 47408, USA

¹⁰ Institut de Recherches Subatomiques, Strasbourg, France

- ¹¹ Ohio State University, Columbus, OH 43210, USA
- ¹² SUBATECH, Nantes, France
- ¹³ Wayne State University, Detroit, MI 48201, USA
- ¹⁴ Yale University, New Haven, CT 06520, USA
- ¹⁵ University of Rajasthan, Jaipur 302 004, India
- ¹⁶ University of Jammu, Jammu 180 001, India
- ¹⁷ University of Washington, Seattle, WA 98195, USA
- ¹⁸ Brookhaven National Laboratory, Upton, NY 11973, USA
- ¹⁹ Lawrence Berkeley National Laboratory, Berkeley, CA 94720, USA
- ²⁰ Rice University, Houston, TX 77251, USA
- ²¹ Moscow Engineering Physics Institute, Moscow Russia
- ²² Nuclear Physics Institute AS CR, 250 68 Řež/Prague, Czech Republic
- ²³ Argonne National Laboratory, Argonne, IL 60439, USA
- ²⁴ Shanghai Institute of Applied Physics, Shanghai 201800, People's Republic of China
- ²⁵ University of Science & Technology of China, Hefei 230026, People's Republic of China
- ²⁶ University of California, Los Angeles, CA 90095, USA
- ²⁷ Tsinghua University, Beijing 100084, People's Republic of China
- ²⁸ Creighton University, Omaha, NE 68178, USA
- ²⁹ Pusan National University, Pusan, Korea
- ³⁰ Universidade de Sao Paulo, Sao Paulo, Brazil
- ³¹ University of California, Berkeley, CA 94720, USA
- ³² University of Texas, Austin, TX 78712, USA
- ³³ Institute of High Energy Physics, Protvino, Russia
- ³⁴ University of Frankfurt, Frankfurt, Germany
- ³⁵ Max-Planck-Institut für Physik, Munich, Germany
- ³⁶ Massachusetts Institute of Technology, Cambridge, MA 02139-4307, USA
- ³⁷ Institute of Particle Physics, CCNU (HZNU), Wuhan 430079, People's Republic of China
- ³⁸ Texas A&M University, College Station, TX 77843, USA
- ³⁹ Warsaw University of Technology, Warsaw, Poland
- ⁴⁰ Valparaiso University, Valparaiso, IN 46383, USA
- ⁴¹ Pennsylvania State University, University Park, PA 16802, USA
- ⁴² Purdue University, West Lafayette, IN 47907, USA
- ⁴³ California Institute of Technology, Pasadena, CA 91125, USA
- ⁴⁴ Institute of Modern Physics, Lanzhou, People's Republic of China
- ⁴⁵ Carnegie Mellon University, Pittsburgh, PA 15213, USA
- ⁴⁶ City College of New York, New York City, NY 10031, USA
- ⁴⁷ Institute of Physics, Bhubaneswar 751 005, India
- ⁴⁸ Indian Institute of Technology, Mumbai, India
- ⁴⁹ University of Zagreb, Zagreb, HR-10002, Croatia
- ⁵⁰ Michigan State University, East Lansing, MI 48824, USA

Received 14 November 2006

Published 30 March 2007

Online at stacks.iop.org/JPhysG/34/799

Abstract

Measurements of two-particle correlations on transverse momentum p_t for Au–Au collisions at $\sqrt{s_{NN}} = 130$ GeV are presented. Significant large-momentum-scale correlations are observed for charged primary hadrons with $0.15 \leq p_t \leq 2$ GeV/ c and pseudorapidity $|\eta| \leq 1.3$. Such correlations were not observed in a similar study at lower energy and are not predicted by theoretical collision models. Their direct relation to mean- p_t fluctuations measured in the same angular acceptance is demonstrated. Positive correlations are observed for pairs of particles which have large p_t values while negative correlations occur for pairs in which one particle has large p_t and the other has much lower p_t . The correlation amplitudes per final state particle increase with

collision centrality. The observed correlations are consistent with a scenario in which the transverse momentum of hadrons associated with initial-stage semi-hard parton scattering is dissipated by the medium to lower p_t .

(Some figures in this article are in colour only in the electronic version)

1. Introduction

Studying two-particle correlations and event-wise fluctuations can provide essential information about the medium produced in ultrarelativistic heavy ion collisions [1–3]. At the collision energies available at the Relativistic Heavy Ion Collider (RHIC) energetic parton scattering occurs at sufficient rate to enable quantitative studies of in-medium modification of parton scattering and the distribution of correlated charged hadrons associated with those energetic partons. Modification of those correlation structures is expected as the bulk medium produced in ultrarelativistic heavy ion collisions increases in spatial extent and energy density with increasing collision centrality. Analyses of the centrality dependence in Au–Au collisions of high- p_t back-to-back jet angular correlations based on a leading-particle technique (e.g., leading-particle $p_t > 4$ GeV/ c , associated particle $p_t < 4$ GeV/ c) reveal strong suppression for central collisions [4, 5], suggesting the development of a medium which dramatically dissipates momentum. Complementary studies of the lower- p_t bulk medium, its correlation structure on transverse momentum, and how those correlations evolve with collision centrality provide a measure of the momentum transport from the few GeV/ c range to lower p_t of order a few tenths of a GeV/ c where the bulk hadronic production occurs. Such studies are an essential part of understanding the nature of the medium produced in heavy ion collisions at RHIC.

In addition to jet angular correlations at high- p_t substantial nonstatistical fluctuations in event-wise mean transverse momentum $\langle p_t \rangle$ of charged particles from Au–Au collisions were reported by the STAR [6] and PHENIX [7] experiments at RHIC. $\langle p_t \rangle$ fluctuations at RHIC are much larger than those reported at the CERN Super Proton Synchrotron (SPS) with one-tenth the CM energy [8], and were not predicted by theoretical models [6, 9–11]. $\langle p_t \rangle$ fluctuations could result from several sources including collective flow (e.g., elliptic flow [12] when azimuthal acceptance is incomplete), local temperature fluctuations, quantum interference [13], final-state interactions, resonance decays, longitudinal fragmentation [14], and initial-state multiple scattering [15] including hard parton scattering [9] with subsequent in-medium dissipation [16]. $\langle p_t \rangle$ fluctuations can be directly related to integrals of two-particle correlations over the p_t acceptance. Correlations on p_t , by providing differential information, better reveal the underlying dynamics for the observed nonstatistical fluctuations in $\langle p_t \rangle$.

In this paper, we report the first measurements at RHIC of two-particle correlations (based on number of pairs) on two-dimensional (2D) transverse momentum space (p_{t1}, p_{t2}) for all charged particles with $0.15 < p_t < 2$ GeV/ c and $|\eta| < 1.3$ (pseudorapidity) using the $\sqrt{s_{NN}} = 130$ GeV Au–Au collisions observed with the STAR detector [17]. This analysis is intended to reveal the response of the bulk medium to strong momentum dissipation and probe the dynamical origins of $\langle p_t \rangle$ fluctuations. The data used in this analysis are described in section 2 and the analysis method, corrections and errors are discussed in section 3. Models and fits to the data are presented in sections 4 and 5, respectively. A discussion and summary are presented in sections 6 and 7.

2. Data

Data for this analysis were obtained with the STAR detector [17] using a 0.25 T uniform magnetic field parallel to the beam axis. A minimum-bias event sample (123k triggered events) required coincidence of two zero-degree calorimeters (ZDC); a 0–15% of total cross section event sample (217k triggered events) was defined by a threshold on the Central Trigger Barrel (CTB) scintillators, with ZDC coincidence. Event triggering and charged-particle measurements with the Time Projection Chamber (TPC) are described in [17]. Approximately 300k events were selected for use in this analysis. A primary event vertex within 75 cm of the axial centre of the TPC was required. Valid TPC tracks fell within the detector acceptance used here, defined by $0.15 < p_t < 2.0$ GeV/c, $|\eta| < 1.3$ and 2π in azimuth. Primary tracks were defined as having a distance of the closest approach less than 3 cm from the reconstructed primary vertex which included a large fraction of true primary hadrons plus approximately 7% background contamination [18] from weak decays and interactions with the detector material. In addition accepted particle tracks were required to include a minimum of 10 fitted points (the TPC contains 45 pad rows in each sector) and, to eliminate split tracks (i.e., one particle trajectory reconstructed as two or more tracks), the fraction of space points used in a track fit relative to the maximum number expected was required to be $>52\%$. Particle identification was not implemented but charge sign was determined. Further details associated with track definitions, efficiencies and quality cuts are described in [18, 19].

3. Data analysis

3.1. Analysis method

Our eventual goal is to determine the complete structure of the six-dimensional two-particle correlation for all hadron pair charge combinations. Towards this goal the two-particle momentum space was projected onto 2D subspace (p_{t1}, p_{t2}) by integrating the pseudorapidity and azimuth coordinates $(\eta_1, \eta_2, \phi_1, \phi_2)$ over the detector acceptance for this analysis, $|\eta| < 1.3$ and full 2π azimuth. Projection onto 2D subspace (p_{t1}, p_{t2}) is achieved by filling 2D binned histograms of the number of pairs of particles for all values of η, ϕ within the acceptance. Complementary correlation structures on relative pseudorapidity and azimuth coordinates with integration over transverse momentum acceptance are reported in [20, 21].

The quantities obtained here are ratios of normalized histograms of *sibling* pairs (particles from the same event) to *mixed-event* pairs (each particle of the pair is from a different, but similar event) in an arbitrary 2D bin with indices a, b representing the values of p_{t1} and p_{t2} (see discussion below). The normalized pair-number ratio \hat{r}_{ab} introduced in [22] is here defined by

$$\hat{r}_{ab} \equiv \hat{n}_{ab,\text{sib}} / \hat{n}_{ab,\text{mix}}, \quad (1)$$

where $\hat{n}_{ab,\text{sib}} = n_{ab,\text{sib}} / \sum_{ab} n_{ab,\text{sib}}$ (sum over all 2D bins), $\hat{n}_{ab,\text{mix}} = n_{ab,\text{mix}} / \sum_{ab} n_{ab,\text{mix}}$, and $n_{ab,\text{sib}}$ and $n_{ab,\text{mix}}$ are the inclusive number of sibling and mixed-event pairs, respectively, in 2D bin a, b . Histograms and ratios \hat{r}_{ab} were constructed for each charge-sign combination: $(+, +)$, $(-, -)$, $(+, -)$ and $(-, +)$. Ratio \hat{r}_{ab} is approximately 1, while difference $(\hat{r}_{ab} - 1)$ measures correlation amplitudes and is the quantity reported here.

The exponential decrease in particle yield with increasing p_t degrades the statistical accuracy of \hat{r}_{ab} at larger transverse momentum, thus obscuring the statistically significant correlation structures there. In order to achieve approximately uniform statistical accuracy across the full p_t domain considered here, nonuniform bin sizes on p_t were used. This was done by noting that the charged hadron p_t distribution, $dN/p_t dp_t$, for Au–Au collisions at

$\sqrt{s_{NN}} = 130$ GeV is approximately exponential for $0.15 < p_t < 2$ GeV/c [18] and by dividing the running integral of that exponential distribution into equal bin sizes. This procedure provides a convenient mapping from p_t to function $X(p_t) \equiv 1 - \exp\{-(m_t - m_0)/0.4 \text{ GeV}\}$ where $0 < X < 1$, $m_t = \sqrt{p_t^2 + m_0^2}$, and m_0 (here assumed to be the pion mass m_π) is a mapping parameter from coordinate p_t to X .⁵¹ Equal bin sizes in X therefore have approximately the same number of sibling pairs. For this analysis 25 equal width bins on X from $X(p_t = 0.15 \text{ GeV}/c) = 0.15$ to $X(p_t = 2.0 \text{ GeV}/c) = 0.99$ were used⁵².

Normalized pair-number ratios were formed from subsets of events with similar centrality (multiplicities differ by ≈ 100 , except ≈ 50 for the most-central event class) and primary-vertex location (within 7.5 cm along the beam axis) and combined as weighted (by sibling pair number) averages within each centrality class. The normalized pair-number ratios for each charge-sign were combined to form like-sign (LS: ++, --) and unlike-sign (US: +-, -+) quantities. The final correlations reported here were averaged over all four charge-sign quantities, resulting in the correlation structures common to all charge-sign combinations. Hence we refer to these final results as *charge-independent* (CI = LS + US) correlations even though they are constructed from quantities which depend on the charge signs of the hadron pairs. The correlation measure reported here is therefore the CI combination for $\hat{r}[X(p_{t1}), X(p_{t2})] - 1$.

Deviations of event-wise $\langle p_t \rangle$ fluctuations from a central-limit theorem [24, 25] are measured by the scale-dependent (i.e., η, ϕ bin sizes) variance difference $\Delta\sigma_{p_t:n}^2$ introduced in [6], where it was evaluated at the STAR (η, ϕ) detector acceptance scale. $\Delta\sigma_{p_t:n}^2$ can be expressed as a *weighted integral* on (p_{t1}, p_{t2}) of the pair-density difference $\rho_{\text{sib}} - \rho_{\text{mix}}$, where two-particle densities ρ_{sib} and ρ_{mix} are approximated by the event-averaged number of sibling and mixed-event pairs per 2D bin, respectively. Both densities are normalized to the event-averaged total number of pairs. $\Delta\sigma_{p_t:n}^2$ can be rewritten exactly as a discrete sum over p_t products [24] (first line in equation (2) below), and the summations approximated in turn by the weighted integral of the pair-density difference (second line in equation (2)) according to

$$\begin{aligned} \Delta\sigma_{p_t:n}^2 &\equiv \frac{1}{\bar{N}} \frac{1}{\epsilon} \sum_{j=1}^{\epsilon} \sum_{i \neq i'=1}^{N_j} (p_{tji} p_{tji'} - \hat{p}_t^2) \\ &\approx \frac{1}{\bar{N}} \iint dp_{t1} dp_{t2} p_{t1} p_{t2} (\rho_{\text{sib}} - \rho_{\text{mix}}) \\ &\equiv \hat{p}_t^2 \bar{N} \langle r(p_{t1}, p_{t2}) - 1 \rangle, \end{aligned} \quad (2)$$

where the weighted average $\langle r(p_{t1}, p_{t2}) - 1 \rangle$ is defined in the last line with weight $p_{t1} p_{t2} \rho_{\text{mix}}(p_{t1}, p_{t2})$ and the integral of ρ_{mix} , $\iint dp_{t1} dp_{t2} p_{t1} p_{t2} \rho_{\text{mix}}$, is $\bar{N}^2 \hat{p}_t^2$.⁵³ In equation (2) N_j is the event-wise number of accepted particles, \bar{N} is the mean of N_j in the centrality bin, ϵ is the number of events, j is the event index, \hat{p}_t is the mean of the ensemble-average p_t distribution (all accepted particles from all events in a centrality bin), and i, i' are particle indices. Equation (2) relates nonstatistical $\langle p_t \rangle$ fluctuations at the acceptance scale to the weighted integral of $\rho_{\text{sib}} - \rho_{\text{mix}}$, the latter difference being related to

⁵¹ Function $X(p_t)$ permits a fully analytic description of the data in $[X(p_{t1}), X(p_{t2})]$ space using the fitting model in (p_{t1}, p_{t2}) space described in section 4. Choice $m_0 = m_\pi \approx T$ emphasizes the soft part of the m_t spectrum in mapping from p_t to $X(p_t)$ where a temperature model is more appropriate.

⁵² Other mappings are possible. For example, in analysis of transverse jets, transverse rapidity $y_t(p_t) \equiv \ln\{(m_t + p_t)/m_0\}$ is optimal for comparing longitudinal and transverse fragment distributions.

⁵³ The weighted integral of ρ_{mix} corresponds to \bar{N} times the second term in the first line of equation (2). The event ensemble average number of mixed-event pairs for that term is $\overline{N(N-1)} = \bar{N}^2 - \bar{N} + \sigma_N^2$, where σ_N^2 is the variance of the multiplicity distribution, assumed to be Poisson, such that $\sigma_N^2 = \bar{N}$.

the two-particle number correlation density. In the present analysis we measure normalized pair-ratio distributions $\hat{r}[X(p_{t1}), X(p_{t2})]$ exhibiting two-particle number correlations on p_t which correspond to excess $\langle p_t \rangle$ fluctuations.

3.2. Corrections and centrality

Corrections were applied to ratio \hat{r} for two-particle reconstruction inefficiencies due to overlapping space points in the TPC (two trajectories merged into one reconstructed track) and intersecting trajectories which cross paths within the TPC and are reconstructed as more than two tracks. These corrections were implemented using two-track proximity cuts⁵⁴ at various radial positions in the TPC in both the longitudinal (drift) and transverse directions (approximately along the pad rows). The track pair cuts were applied to both ρ_{sib} and ρ_{mix} as in HBT analyses [13]. Small-momentum-scale correlation structures due to quantum interference, Coulomb and strong final-state interactions [13] were suppressed by eliminating sibling and mixed-event track pairs ($\sim 3\%$ of total pairs) with $|\eta_1 - \eta_2| < 0.3$, $|\phi_1 - \phi_2| < \pi/6$ (azimuth), $|p_{t1} - p_{t2}| < 0.15$ GeV/c, if $p_t < 0.8$ GeV/c for either particle. The small-momentum-scale correlation (SSC) structures are most prominent in the lower- p_t domain of the 2D (p_{t1}, p_{t2}) space along the $p_{t1} = p_{t2}$ diagonal and were shown to be similar in amplitude and location to simulations [26] which account for quantum interference correlations and Coulomb final-state interaction effects using pair weights determined by HBT analyses for these data [13]. The preceding cuts were optimized [19] to eliminate the SSC structure without affecting the large-momentum-scale correlation (LSC) structure which is of primary interest here. The track-pair cuts generally have small effects on the LSC; uncertainties which result from application of these cuts are discussed in section 3.3 and are negligible compared to the large momentum scale structures studied here.

Four centrality classes labelled (a)–(d) for central to peripheral were defined by cuts on TPC track multiplicity N within the acceptance by (d) $0.03 < N/N_0 < 0.21$, (c) $0.21 < N/N_0 < 0.56$, (b) $0.56 < N/N_0 < 0.79$ and (a) $N/N_0 > 0.79$, corresponding respectively to the approximate fraction of total cross section ranges 40–70%, 17–40%, 5–17% and 0–5%. N_0 is the end-point⁵⁵ of the minimum-bias multiplicity distribution.

The centrality dependence of quantity $\hat{r} - 1$ is shown in figure 1 as perspective views for the four centrality classes used here. This correlation measure represents the number of correlated particle pairs per final-state pair in each 2D bin, and therefore contains a dilution factor $1/\bar{N}$ relative to the LSC measure presented in [21], $\bar{N}(\hat{r} - 1)$ whose amplitudes are of order one. The structures in figure 1 are therefore numerically a few *permil* for central Au–Au collisions but are highly significant statistically as seen by comparing to the statistical errors. The dominant features in figure 1 are (1) a large-momentum-scale correlation ‘saddle’ structure with positive curvature along the $X(p_t)_\Sigma \equiv X(p_{t1}) + X(p_{t2})$ sum direction from $[X(p_{t1}), X(p_{t2})] (0, 0)$ to $(1, 1)$ and a corresponding negative curvature along the $X(p_t)_\Delta \equiv X(p_{t1}) - X(p_{t2})$ difference direction from $[X(p_{t1}), X(p_{t2})] (0, 1)$ to $(1, 0)$, and (2) a narrow peak structure at large $X(p_t)$ ($p_t > 0.6$ GeV/c). With increasing centrality the negative curvature of the LSC saddle shape along the difference variable increases in magnitude, the positive curvature along the sum variable decreases, and the magnitude of the peak at large $X(p_t)$ also decreases. Without the SSC cuts a relatively small peaked structure with amplitude of order 0.004 (peripheral) to

⁵⁴ Two-track merging cuts required the average separation distance ≥ 10 cm based on two-track separations at nine radial positions in the TPC. Two tracks which cross within the TPC with separations less than 10 cm (z) and 30 cm (azimuth) at mid-radius from the TPC axis were also excluded.

⁵⁵ N_0 , the half-maximum point at the end of the minimum-bias distribution plotted as $d\sigma/dN^{1/4}$, is an estimator on N for the maximum number of participants; $N_{\text{part}}/N_{\text{part,max}} \simeq N/N_0$ within 4%.

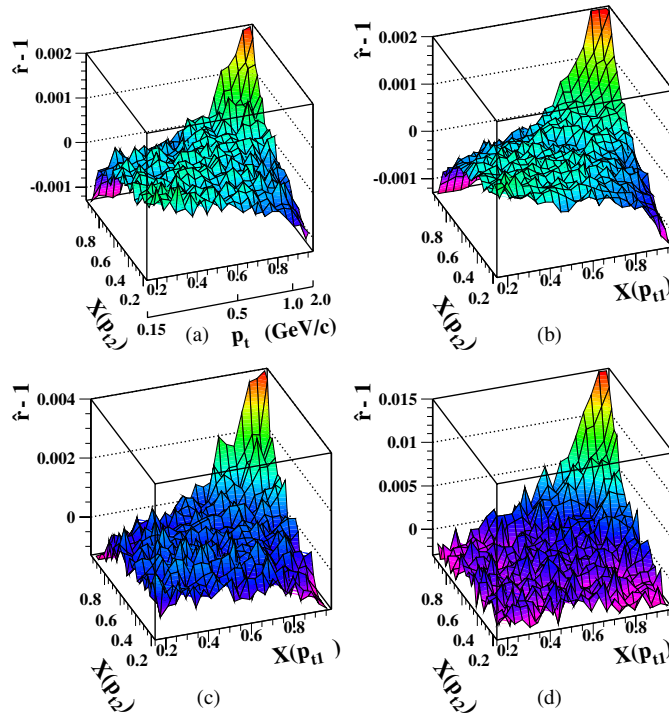


Figure 1. Symmetrized pair-density net ratios $\hat{r}[X(p_{t1}), X(p_{t2})] - 1$ for all nonidentified charged primary particles for (a) most-central, (b) mid-central, (c) mid-peripheral, and (d) peripheral Au–Au collision events at $\sqrt{s_{NN}} = 130$ GeV/c. Note the scale change for panels (c) and (d) and auxiliary p_t scale in units GeV/c in panel (a). SSC were removed using track pair cuts (see text). Errors are discussed in section 3.3.

0.0005 (central) is present for $X(p_t) < 0.3$ ($p_t < 0.25$ GeV/c) which weakens in amplitude but visibly persists to $X(p_t) < 0.6$ ($p_t < 0.5$ GeV/c).

An upper limit estimate for resonance contributions was obtained using Monte Carlo simulations [26] assuming 70% of the primary charged particle production is from resonance decays. The correlations were simulated by populating the events with a sufficient number of ρ^0 , ω two-body decays to account for 70% of the observed multiplicity. These two-body decay processes produced a small saddle-shape correlation with curvature opposite to the data and amplitude at the corners approximately 0.0002 for the most-central data, increasing as $1/\bar{N}$ for the remaining centrality bins. The saddle-shape structures in figure 1 cannot be explained with resonance decays.

The same analysis applied to Pb–Pb collisions in $1.1 < y_{cm} < 2.6$ at the CERN SPS did not reveal any statistically significant CI correlations [27] when SSC (see section 3.2) were removed with pair cuts. The analysis in [28] of proton + proton and various nucleus + nucleus collision data from the CERN SPS for $1.1 < y_{cm} < 2.6$ without those pair cuts revealed SSC peaks at low $X(p_t)$ along the $X(p_t)_\Sigma$ direction.

3.3. Error analysis

Per-bin statistical errors for $\hat{r} - 1$ in figure 1 range from ~ 6 –9% of the maximum correlation amplitude for each centrality (typically 0.00015, 0.00011, 0.00035 and 0.001 for centralities

(a)–(d) respectively) and are approximately uniform, by design, over the 2D domain on $X(p_t)$. Statistical errors for $\bar{N}(\hat{r} - 1)$ ($\sim 0.1 - 0.15$) are less dependent on centrality.

Systematic errors were estimated as in [6, 21] and are dominated by the 7% non-primary background contamination [18] whose correlation with primary particles is unknown. The upper limit on the systematic error from this source was estimated by assuming that the number of correlated pairs associated with background-primary pairs of particles could range from zero up to the amount which would occur among 7% of the primary particles and the remaining primaries. This conservative assumption produces an overall $\pm 7\%$ uncertainty relative to the correlation amplitudes in figure 1 throughout the domain for $X(p_{t1,2}) > 0.4$. This error increases to $\pm 16\%$ at lower $X(p_t)$ where the contamination fraction is larger and is about $\pm 12\%$ in the off-diagonal corners of the $[X(p_{t1}), X(p_{t2})]$ domain. Multiplicative factors for quantity $\hat{r} - 1$ which correct for the non-primary background contamination range from 1.0, assuming that background-primary particle pairs are correlated and increase both $\hat{n}_{ab,sib}$ and $\hat{n}_{ab,mix}$ by $2 \times 7\% = 14\%$, to 1.14 if background-primary particle pairs are uncorrelated but the non-primary background contributes 14% to $\hat{n}_{ab,mix}$. Multiplication of the data in figure 1 by average factor 1.07 provides an estimate of the background corrected correlation amplitudes.

Additional sources of systematic error were evaluated. Uncertainty in the two-track inefficiency corrections have modest effects along the $X(p_{t1}) = X(p_{t2})$ diagonal ($< 2\%$) and are negligible elsewhere. Tracking anomalies caused when particle trajectories intersect the TPC high-voltage central membrane significantly affect the $X(p_{t1,2}) < 0.2$ domain corresponding to the single bin at lowest $X(p_t)$, and the diagonal bins for $X(p_{t1,2}) < 0.4$ by 20%. Final multiplicative correction estimates (not applied in figure 1) and total systematic errors for $\hat{r} - 1$ varied respectively from 1.07 and $\pm 7\%$ for $X(p_{t1,2}) > 0.4$ up to 1.16 and $\pm 16\text{--}20\%$ for $X(p_{t1,2}) < 0.4$ and 1.12 and $\pm 12\%$ in the off-diagonal corners (i.e., near (0, 1) and (1, 0)).

Other potential sources of systematic error were studied and determined to have negligible effects including primary vertex position uncertainty perpendicular to the beam direction, variation of tracking acceptance and efficiency with primary vertex location along the axis of the TPC, TPC drift speed and/or timing-offset fluctuation, sporadic outages of TPC read-out electronic components, angular resolution, multiplicity and primary vertex position bin sizes used for producing mixed events, and charge sign dependence of the tracking efficiency. Conversion electron contamination is suppressed by the lower p_t acceptance cut and also by the pair cuts described in section 3.2 and also makes negligible contribution to the systematic error.

4. Modelling one- and two-particle distributions on p_t

Two features dominate the data in figure 1: (1) a large-momentum scale saddle shape and (2) a peak at large $X(p_{t1})$ and $X(p_{t2})$. In this section, results from Monte Carlo collision models are analysed in order to gain insight into the dynamical origin(s) of these two correlation structures in the data. Based on this study an analytical function is obtained which accurately describes the saddle shape and in section 5 this function is used to fit the 2D correlation data.

The high-energy nuclear collision model Hijing [9], which includes longitudinal colour-string fragmentation and perturbative quantum chromodynamics (pQCD) based jet production and jet quenching, exhibits a significant correlation structure at higher p_t [$X(p_{t1}) + X(p_{t2}) > 1.6$] as shown in the left-hand panel of figure 2 for central Au–Au collisions. The predictions, which include jet production with jet quenching (default parameters) are qualitatively different from the data in figure 1, failing to produce any saddle-shape, but suggest the type of correlation structure produced by jets. The general structure of the Hijing predictions suggests that the

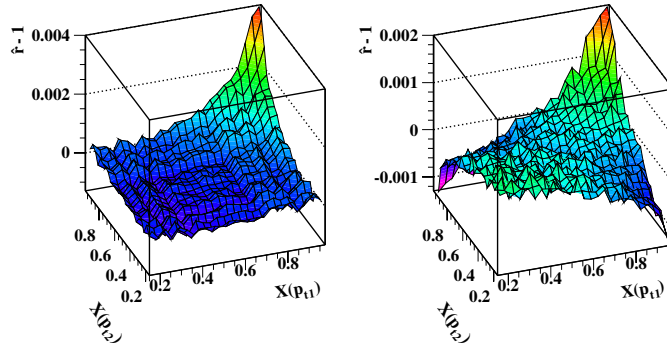


Figure 2. Symmetrized pair-density ratio $\hat{r}[X(p_{t1}), X(p_{t2})] - 1$ for unidentified charged particles and for central Au–Au collisions. Left panel: default Hijing [9] with jet quenching, Right panel: a Monte Carlo model [26] which simulates event-wise global temperature fluctuations (see text).

peaks in the data at higher $X(p_t)$ are at least partly due to initial-state partonic scattering and fragmentation. Other theoretical models which combine initial-state parton scattering, energy loss, dissipation, rescattering and recombination [11, 29] may eventually explain these correlation data, but relevant predictions are not available at this time.

The saddle-shape correlation spans the entire momentum scale studied here, suggesting event-wise fluctuations of global event characteristics (e.g. temperature and/or collective velocity of the bulk medium) as a possible source. If heavy ion collisions at RHIC thermalize then an ensemble of collision events would be characterized by a distribution of event-wise equilibrium temperatures reflecting event-to-event fluctuations in the initial conditions and time evolution of each colliding system. Based on this idea the transverse momentum correlations for an ensemble of such events can be predicted using a Monte Carlo model in which charged particle production is generated by sampling the inclusive single-particle (p_t, η, ϕ) distribution obtained from the data. At mid-rapidity the inclusive distribution on p_t for $0.15 \leq p_t \leq 2$ GeV/c is well approximated by $\exp(-m_t/T) \equiv \exp(-\beta m_t)$ [18] where T is an effective temperature [30] or inverse slope parameter and $\beta = 1/T$. Events were generated by sampling $\exp(-m_t/T)$ where T fluctuates randomly from event-to-event according to a Gaussian distribution about mean value $T_0 = 1/\beta_0$; T_0 was determined by the measured p_t spectrum.

The result of this Monte Carlo model for central Au–Au collisions at 130 GeV is shown in the right-hand panel of figure 2 where the mean and standard deviation (Gaussian sigma) of the event-wise temperature distribution are $T_0 = 200$ MeV and $\sigma_T/T_0 = 1.5\%$. The predicted correlations are not sensitive to T_0 but the overall correlation amplitude is directly sensitive to σ_T/T_0 which was adjusted to approximate the overall amplitude of the data in figure 1(a). The global temperature fluctuation model accurately describes the saddle-shape. An analytical function based on this approach is derived in the remainder of this section and is used in the following section (section 5) to fit the data.

We seek an analytical representation of the LSC saddle-shape structure of the data in figure 1 that is both mathematically compact and physically motivated in order to conveniently characterize the centrality dependence and to infer thermodynamic properties of the medium. The above Monte Carlo results indicate that a successful representation should involve an averaging over the inverse slope parameter. In general the inverse temperature β can vary from event-to-event as well as internally within each event, reflecting the possibility of relative ‘hot spots’ and ‘cold spots’ in the final-state particle distributions. The number, location in

source coordinates (e.g., η_z —spacetime rapidity [30] and φ —azimuth), amplitude, and angular extent of these perturbations in β may vary for each event. In addition, for realistic collision systems both thermal and collective motions are involved such that parameter β becomes an inverse *effective* temperature [30] where fluctuations in β could result from fluctuations in the local temperature of the flowing medium, the collective flow velocity itself, or a combination of both effects⁵⁶. Event-wise effective temperature is therefore represented by distribution $T(\eta_z, \varphi)$ on source coordinates η_z and φ , and similarly for $\beta(\eta_z, \varphi)$.

The momentum of a particle at η_z, φ in the final stage of the collision system is obtained by sampling thermal distribution $\exp[-m_t/T(\eta_z, \varphi)] = \exp[-\beta(\eta_z, \varphi)m_t]$ as illustrated in the diagram in figure 3(a). In general the histogram of sampled $T(\eta_z, \varphi)$ or $\beta(\eta_z, \varphi)$ values for all particles in all events in the event ensemble, $g_1(\beta)$, could be like the generic peaked distribution in figure 3(b) with mean β_0 and standard deviation σ_β . The inclusive m_t distribution is then obtained by convoluting thermal distribution $\exp[-\beta(m_t - m_0)]$ with $g_1(\beta)$ given by

$$\frac{dN}{m_t dm_t} = A \int_0^\infty d\beta g_1(\beta) e^{-\beta(m_t - m_0)} \quad (3)$$

where A is a normalization constant. The global temperature fluctuation model is recovered when $T(\eta_z, \varphi)$ is independent of source coordinate but varies from event-to-event.

In the Monte Carlo model event-wise $T = 1/\beta$ was obtained by sampling a Gaussian distribution. It is therefore reasonable to represent $g_1(\beta)$ by a peaked distribution which is here assumed to be a gamma distribution [31] in order to obtain an analytic solution of the integral in equation (3) given by

$$\frac{dN}{m_t dm_t} = A/[1 + \beta_0(m_t - m_0)/n_{\text{fluct}}]^{n_{\text{fluct}}}, \quad (4)$$

a Lévy distribution [32], where $1/n_{\text{fluct}} = \sigma_\beta^2/\beta_0^2$ is the relative variance of $g_1(\beta)$. The finite width of $g_1(\beta)$ produces a net increase in the yield at higher m_t as illustrated in figure 3(c). We emphasize that any finite-width peaked function $g_1(\beta)$ results in an m_t distribution which decreases less rapidly with increasing m_t than thermal spectrum $e^{-\beta_0 m_t}$. The assumption of a gamma distribution for $g_1(\beta)$ is therefore not essential but is used for mathematical convenience and is justified by the capability of the m_t distribution in equation (4) to describe the inclusive data. We note however that deviations of the measured m_t distribution from a thermal spectrum, quantified by exponent n in the power-law m_t distribution [18], can result from transverse expansion [30] in addition to local and event-to-event fluctuations in $\beta(\eta_z, \varphi)$ assumed in deriving equations (3) and (4). Consequently, fitting the $1/m_t dN/dm_t$ spectra to obtain the power-law exponent n cannot by itself determine the relative variance of the effective temperature distribution, $1/n_{\text{fluct}}$, which is related to the degree of equilibration.

Similarly the two-particle distribution on (m_{t1}, m_{t2}) is obtained by convoluting the two-particle thermal distribution $\exp[-\beta_1(m_{t1} - m_0)]\exp[-\beta_2(m_{t2} - m_0)]$ with the 2D distribution of pairs of inverse effective temperature parameters (β_1, β_2) , where particles 1 and 2 sample local thermal distributions determined by $\beta(\eta_{z1}, \varphi_1)$ and $\beta(\eta_{z2}, \varphi_2)$, respectively (see figure 3(a)). The distribution of (β_1, β_2) for all pairs of particles used in all events in the ensemble defines a 2D histogram and 2D distribution, $g_2(\beta_1, \beta_2)$, illustrated in figure 3, panels (d)–(f) for three hypothetical cases. If the event ensemble distribution on β has finite width ($\sigma_\beta > 0$), but is point-to-point uncorrelated within each event, then $g_2(\beta_1, \beta_2)$ is symmetric on β_1 versus β_2 (zero covariance) as shown in figure 3(d). For uncorrelated β fluctuations or for mixed-event pairs, g_2 factorizes as $g_2(\beta_1, \beta_2) = g_1(\beta_1)g_1(\beta_2)$, implying zero covariance. On

⁵⁶ Analysis of the measurements presented here cannot distinguish between fluctuating temperature or flow velocity which would require identified particle mass at higher p_t and over the large η, ϕ acceptance of the STAR TPC.

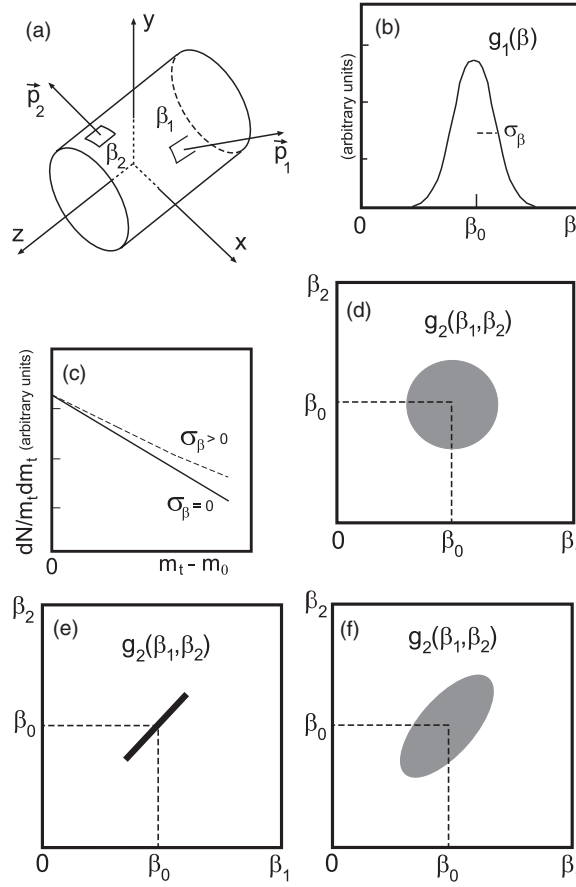


Figure 3. Diagrams illustrating the temperature fluctuation model. Panel (a): source coordinates with two final state particles sampling local inverse temperatures $\beta_1 = \beta(\eta_{z1}, \varphi_1)$ and $\beta_2 = \beta(\eta_{z2}, \varphi_2)$. Panel (b): distribution $g_1(\beta)$ of sampled β values for all particles in all events of a centrality bin with mean β_0 and standard deviation σ_β . Panel (c): thermal model inclusive charged particle yield $dN/m_t dm_t$ at mid-rapidity versus $m_t - m_0$ with no temperature fluctuations ($\sigma_\beta = 0$, solid line) and with temperature fluctuations ($\sigma_\beta > 0$, dashed line). Panel (d): 2D distribution, $g_2(\beta_1, \beta_2)$, of sampled pairs $\beta(\eta_{z1}, \varphi_1)$ and $\beta(\eta_{z2}, \varphi_2)$ when there are no point-to-point temperature correlations within each source but large temperature variations within each event (non-equilibrated sources). Panel (e): same as (d) except for global temperature fluctuations where each event is equilibrated but the equilibrium temperature fluctuates from event-to-event. Panel (f): same as (d) except point-to-point temperature correlations occur within each event as evidenced by the positive covariance of distribution $g_2(\beta_1, \beta_2)$.

the other hand, if every event is thermally equilibrated, then each pair of particles from a given event samples the same value of β where $\beta_1 = \beta_2$. For this case (global temperature fluctuation model) $g_2(\beta_1, \beta_2)$ limits to a diagonal line distribution illustrated in figure 3(e) and given by $g_2(\beta_1, \beta_2) \propto g'_1(\beta_1)\delta(\beta_1 - \beta_2)$, where $\delta(\beta_1 - \beta_2)$ is a Dirac delta-function. In this case g_2 has maximum covariance and represents the conventional picture of an ensemble of equilibrated events with event-wise fluctuations in the global temperature. In general $g_2(\beta_1, \beta_2)$ may have an intermediate covariance as illustrated in figure 3(f). In this case if $g_2(\beta_1, \beta_2)$ is expressed as a product of a gamma distribution on the sum direction, $\beta_\Sigma = \beta_1 + \beta_2$ multiplied by a

Gaussian on $\beta_\Delta = \beta_1 - \beta_2$ (for mathematical convenience), then an analytic expression for the two-particle distribution results, given by a 2D Lévy distribution

$$F_{\text{sib}} \propto \left(1 + \frac{\beta_0 m_{t\Sigma}}{2n_\Sigma}\right)^{-2n_\Sigma} \left[1 - \left(\frac{\beta_0 m_{t\Delta}}{2n_\Delta + \beta_0 m_{t\Sigma}}\right)^2\right]^{-n_\Delta} \quad (5)$$

on sum and difference variables $m_{t\Sigma} \equiv m_{t1} + m_{t2} - 2m_0$ and $m_{t\Delta} \equiv m_{t1} - m_{t2}$. Inverse exponents $1/n_\Sigma$ and $1/n_\Delta$ are the relative variances of $g_2(\beta_1, \beta_2)$ along sum and difference variables β_Σ and β_Δ respectively, and $\Delta(1/n)_{\text{tot}} \equiv 1/n_\Sigma - 1/n_\Delta$ is the relative *covariance* of g_2 ,⁵⁷ measuring velocity/temperature correlations. For the examples in panels (d), (e) and (f) of figure 3, $1/n_\Sigma = 1/n_\Delta$, $1/n_\Sigma > 0$ and $1/n_\Delta = 0$, and $1/n_\Sigma > 1/n_\Delta > 0$, respectively. Mixed-event pair distribution $F_{\text{mix}}(p_{t1}, p_{t2})$, a product of one-dimensional Lévy distributions (equation (4)), has the form of equation (5) but with $n_\Sigma = n_\Delta = n_{\text{fluct}}$.

Ratio

$$r_{\text{model}} \equiv F_{\text{sib}}/F_{\text{mix}}, \quad (6)$$

referred to as a 2D Lévy saddle, predicts a saddle-shape when $g_2(\beta_1, \beta_2)$ has nonzero covariance and is the analytical quantity to be compared to data. It can be tested by comparison to the data in figure 1 via chi-square fits. We emphasize for this 2D case that any peaked function $g_2(\beta_1, \beta_2)$ with *nonzero covariance* results in a 2D saddle shape distribution for r_{model} . The gamma distribution times Gaussian 2D model for g_2 was chosen for mathematical convenience but it is reasonable given the form of the measured event-wise $\langle p_t \rangle$ distribution. The variance of g_2 along the difference direction β_Δ measures the average degree of equilibration of the events in the ensemble. Relative variance *differences* $\Delta(1/n)_\Sigma \equiv (1/n_\Sigma - 1/n_{\text{fluct}})$ and $\Delta(1/n)_\Delta \equiv (1/n_\Delta - 1/n_{\text{fluct}})$ measure the saddle *curvatures* of r_{model} (and hence the data) along sum and difference directions at the origin, and are the quantities best determined by these fits. Sensitivity to the magnitudes of the relative variances $1/n_\Sigma$ and $1/n_\Delta$ is discussed in the next section.

5. Analytical model fits

Data in figure 1 (excluding peak region $X(p_t)_\Sigma > 1.6$) were fitted with $r_{\text{model}} - 1 + \tilde{C}$ by varying parameters n_Σ, n_Δ and \tilde{C} (offset). Parameters $\beta_0 = 5 \text{ GeV}^{-1}$ and $m_0 = m_\pi$ were fixed by the (pion dominated) inclusive single-particle p_t spectrum for $p_t < 1 \text{ GeV}/c$. The fits are insensitive to the absolute value of $1/n_{\text{fluct}}$; its value was fixed as follows. Parameter $1/n$ when fitted to the single particle m_t spectrum [18], using an analogue of equation (4) with n_{fluct} replaced by n , accounts for the deviation between the measured distribution and $e^{-\beta m_t}$. In general, both collective radial expansion velocity [30] and effective temperature fluctuations contribute to the curvature (decreasing slope) of the m_t spectrum relative to Boltzmann reference $e^{-\beta m_t}$ at increasing m_t shown by the dashed curve in figure 3(c). Both contributions are included in parameter n in equation (4), when fitted to the single particle distribution, resulting in an apparent variance, $1/n$, given by an incoherent sum of contributions from radial flow, $1/n_{\text{flow}}$, and effective temperature fluctuations, $1/n_{\text{fluct}}$, where $1/n = 1/n_{\text{flow}} + 1/n_{\text{fluct}}$. However, for the effective temperature fluctuation model developed in the preceding section only component $1/n_{\text{fluct}}$ is relevant to the 2D Lévy saddle fit but it is not accessible because fits to correlation data ($\hat{r} - 1$) poorly constrain absolute quantities $1/n_\Sigma$ and $1/n_\Delta$. However, *differences* $\Delta(1/n)_{\Sigma, \Delta}$ are well determined by the saddle curvatures,

⁵⁷ In the context of velocity/temperature fluctuations this quantity measures $\overline{(\beta_1 - \beta_0)(\beta_2 - \beta_0)}/\beta_0^2$, the relative covariance of velocity/temperature fluctuations.

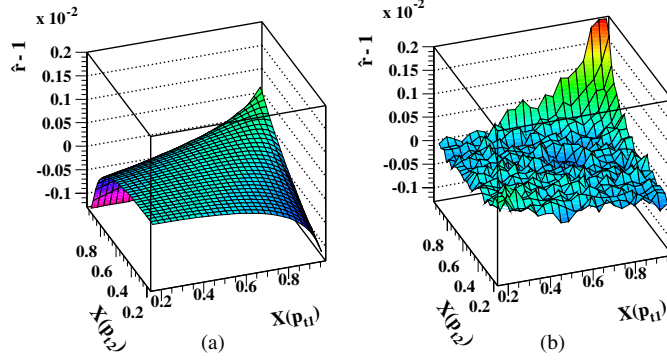


Figure 4. Left: pair-density net ratio $r_{\text{model}}[X(p_{t1}), X(p_{t2})] - 1$ for model fit to mid-central (b) Au–Au collisions. Right: residuals (data—model) for mid-central collisions.

Table 1. Parameters and fitting errors (only) for the 2D velocity/temperature fluctuation model for each centrality bin, (a)–(d) (central–peripheral as in figure 1). Errors (last column) represent fitting uncertainties. Systematic errors are 7–12%.^a Mean multiplicities of used particles in the acceptance, \bar{N} , are listed for each centrality bin. Quantities \mathcal{S} (last row) are correction factors for contamination and tracking inefficiency [6].

Centrality	(d)	(c)	(b)	(a)	Error ^b (%)
\bar{N}	115.5	424.9	790.2	983.0	
$\tilde{C} \times 10^4$	−11.6	−0.820	0.787	0.750	6–14
$\Delta(1/n)_{\Sigma} \times 10^4$	3.54	0.611	0.183	0.118	6–24
$\Delta(1/n)_{\Delta} \times 10^4$	−8.61	−3.33	−2.53	−2.04	6–3
$\Delta(1/n)_{\text{tot}} \times 10^4$	12.2	3.95	2.71	2.16	
χ^2/DoF	$\frac{348}{286}$	$\frac{313}{286}$	$\frac{475}{286}$	$\frac{402}{286}$	
\mathcal{S}	1.19	1.22	1.25	1.27	8 ^c

^a Systematic errors for quantities in figure 5 (right panel), due to systematic uncertainties in the data (7–12%) plus background and efficiency corrections (8%), are 11–14%.

^b Range of fitting errors in per cent from peripheral to central.

^c Systematic error.

nearly independently of the assumed value of $1/n_{\text{fluct}}$ in r_{model} . The maximum value for $1/n_{\text{fluct}}$ corresponds to $1/n = 1/13$ in the no-flow limit, $1/n_{\text{flow}} = 0$, where $n = 13$ is obtained from the Lévy distribution fit to the single particle m_t spectrum [18]. The minimum value of 0.0009 corresponds to that necessitated by the fitted values of $\Delta(1/n)_{\Delta}$ in table 1 in the limit $1/n_{\Delta} \rightarrow 0$. The fits were insensitive to variations of $1/n_{\text{fluct}}$ in this range, intermediate value $1/n_{\text{fluct}} = 0.03$ near the centre of the allowed range provided stable $\Delta(1/n)_{\Sigma}$ and $\Delta(1/n)_{\Delta}$ fit values. Best-fit parameters and χ^2/DoF for the saddle fits are listed in table 1. The model function and residuals for the fit to centrality (b) are shown in figure 4.

Two-dimensional saddle-fit residuals, as in figure 4 (right panel), are approximately constant along directions parallel to the $X(p_{t\Delta}) = X(p_{t1}) - X(p_{t2})$ axis for each value of $X(p_{t\Sigma})$ and are small for $X(p_{t\Sigma}) < 1.5$. The Lévy temperature fluctuation model adequately describes the saddle structure. Residuals from the fit for mid-central events (b) are shown in figure 5 (left panel) projected onto sum variable $X(p_{t\Sigma})$. Errors are included in the data symbols and are smaller than those in figure 4 (right panel) due to bin averaging. Residuals for other centralities are similar, but differ in amplitude. We hypothesize that this residual

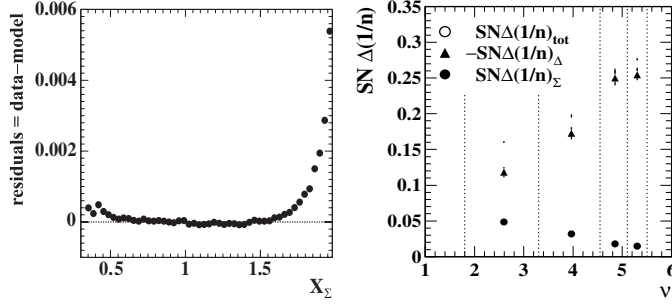


Figure 5. Left: residuals from 2D Lévy saddle fit to mid-central (b) data in figure 1 projected onto sum variable $X(p_t)_\Sigma = X(p_{t1}) + X(p_{t2})$. Right: efficiency-corrected *per-particle* saddle-curvature measures (see footnote 59) on centrality ν : $S\bar{N}\Delta(1/n)_\Sigma$ (dots), $-S\bar{N}\Delta(1/n)_\Delta$ (triangles) and $S\bar{N}\Delta(1/n)_{\text{tot}}$ (open circles). Data symbols include fitting errors only (see footnote 58). Solid lines are linear fits.

structure is due to correlated final-state hadrons associated with initial-state semi-hard parton scattering [33].

Centrality dependences of efficiency-corrected model parameters $S\bar{N}\Delta(1/n)$,⁵⁸ which determine saddle-shape correlation amplitudes in figure 1, are shown in figure 5 (right panel). The linear trends suggested by the solid lines are notable. Multiplication by factor $S\bar{N}$ estimates correlation amplitudes per final state primary particle as discussed below. Centrality measure ν estimates the mean participant path length as the average number of encountered nucleons per participant nucleon in the incident nucleus. For this analysis $\nu \equiv 5.5(N/N_0)^{1/3} \approx 5.5(N_{\text{part}}/N_{\text{part,max}})^{1/3} \approx 2N_{\text{bin}}/N_{\text{part}}$, based on Glauber-model simulations where N_{part} (N_{bin}) is the number of participant nucleons (binary collisions).

The reasons for multiplying the parameters in table 1 by S and \bar{N} are the following. Multiplication of $(\hat{r} - 1)$ by \bar{N} yields the density of correlated pairs *per final-state particle* [21], typically $O(1)$ for all centralities. $\bar{N}(\hat{r} - 1)$ would be independent of centrality if Au–Au collisions were linear superpositions of p–p collisions (participant scaling) because the amplitude of the numerator of $(\hat{r} - 1)$, which is proportional to the density of correlated pairs, would scale with participant number, or in this model with \bar{N} , while the denominator is proportional to \bar{N}^2 . Therefore variation of $\bar{N}(\hat{r} - 1)$ with centrality directly displays the effects of those aspects of Au–Au collisions which do not follow naïve p–p superposition. Factor S is defined as the ratio of true, primary particle yield (i.e., 100% tracking efficiency and no background contamination) estimated for these data in [18] divided by the actual multiplicity used in this analysis corrected for the $\sim 7\%$ background contamination. S is essentially the reciprocal of the charged-particle tracking efficiency, specific for the present analysis. Multiplication by factor $S\bar{N}$ of the parameters in table 1 therefore estimates the correlation amplitudes per final-state particle for 100% tracking efficiency and no background contamination, assuming that the measured correlations include background-primary particle correlations half-way between the limits described in section 3.3. The uncertainty in extrapolating to the true primary particle yield is estimated to be 8%, most of which is due to the 7% systematic uncertainty in the measured charged hadron yield [18]. The combined

⁵⁸ Multiplication by $S\bar{N}$ gives *per-particle*, rather than *per-pair*, correlation amplitudes which better reveal non-trivial centrality dependences for A–A collisions relative to an independent nucleon–nucleon collision superposition hypothesis. For the latter case the rescaled correlation amplitudes would be independent of centrality.

systematic uncertainty for the efficiency corrected amplitudes is from $\pm 11 - 14\%$ across the $X(p_{t1})$ versus $X(p_{t2})$ space.

6. Discussion

Correlations on p_t have two main components, a saddle shape and a peak at higher p_t . By measuring the saddle curvatures we infer the relative covariance of two-point distribution $g_2(\beta_1, \beta_2)$ and hence the average two-point correlation amplitude of the temperature/velocity structure of the composite particle source. We now consider possible dynamical origins of that structure.

The analysis of the saddle-shape produces accurate results for relative variance differences $\Delta(1/n)_\Sigma = (\sigma_{\beta_\Sigma}^2 - \sigma_\beta^2)/\beta_0^2$, $\Delta(1/n)_\Delta = (\sigma_{\beta_\Delta}^2 - \sigma_\beta^2)/\beta_0^2$, and the corresponding $\Delta(1/n)_{\text{tot}} = (\sigma_{\beta_\Sigma}^2 - \sigma_{\beta_\Delta}^2)/\beta_0^2$ for effective temperature fluctuations. The measurements do not constrain the absolute magnitudes of the individual variances, $\sigma_{\beta_\Sigma}^2$ and $\sigma_{\beta_\Delta}^2$. The minimum possible values, consistent with the saddle-shape conditions and the single-particle m_t spectra, correspond to $\sigma_{\beta_\Delta}^2 = 0$ and $1/n_{\text{fluct}} = -\Delta(1/n)_\Delta$, resulting in $\sigma_\beta/\beta_0 \cong \sigma_T/T_0 = 1.4\%$ to 2.9% global event-to-event temperature/velocity fluctuation from central to peripheral collisions, respectively. In this case $1/n \cong 1/n_{\text{flow}}$ and global temperature/velocity fluctuations contribute negligibly to the upward curvature of the $dN/m_t dm_t$ spectrum. The maximum values for the variances correspond to $1/n_{\text{flow}} = 0$, resulting in $1/n_{\text{fluct}} = 1/n$ and $\sigma_\beta/\beta_0 \cong \sigma_T/T_0 = \sqrt{1/n} = 30\%$, where $\sigma_{\beta_\Delta} \sim \sigma_\beta$, corresponding to 30% local temperature/velocity fluctuations within each event, a significantly non-equilibrated system. Thus, local temperature variation could range between 0 and 30%. One can ask what is the source of the fluctuating effective temperature, and is local source velocity rather than temperature a more appropriate quantity?

Given the correlation peaks at higher p_t it is reasonable to offer the hypothesis that the saddle-shape correlation structure in figure 1 results from in-medium modification, specifically momentum dissipation on (p_{t1}, p_{t2}) of a two-particle distribution from fragmenting, semi-hard scattered partons in the initial-stage of the collision. Since no selection was made on leading particle or high- p_t ‘trigger’ particle for these data we refer to the hadrons associated with a semi-hard, initial-state scattered parton as a *minijet* [9, 34]. Minijet production in Au–Au collisions should increase approximately linearly with N_{bin} [35, 36] while the subsequent momentum dissipation should monotonically increase with greater minijet production. Correlation amplitudes per final state particle (the latter approximately proportional to N_{part}) should therefore increase monotonically with mean participant path length $v \cong N_{\text{bin}}/(N_{\text{part}}/2)$, thus providing a basis for experimental tests of this hypothesis.

The linear trends in figure 5 (right panel) therefore support, but do not *require*, a minijet-momentum dissipation mechanism for the observed correlations on p_t . In figure 5 we also observe (1) reduced curvature along the sum direction and (2) increased curvature along the difference direction which may represent respectively transport of semi-hard parton structure to lower p_t and a more correlated bulk medium. Given a minijet interpretation of $S\bar{N}\Delta(1/n)_{\text{tot}}$, the combined trends (1) and (2) represent strong evidence for increased parton dissipation in the more central Au–Au collisions. The present results complement the observed suppression of high- p_t spectra (R_{AA}) [35, 36] and suppression of large angle trigger-particle-associated-particle conditional distributions on $\Delta\phi$ [4, 5] in central Au–Au collisions at RHIC. It is very likely that the lower- p_t fluctuations and correlations reported here are, at least in large part, a consequence of the processes which lead to the above suppressions at higher- p_t .

It is important to note that these correlations on transverse momentum observed at relatively low p_t reveal nominally ‘soft’ structure in relativistic heavy ion collisions which

scales with the number of binary collisions N_{bin} , whereas a low- p_t inclusive quantity such as multiplicity scales with participant number N_{part} . Binary-collision scaling is conventionally thought to be an aspect of high- p_t physics and initial-state scattering. This analysis suggests that substantial effects of initial-state parton scattering are manifest at low p_t in more central heavy ion collisions.

7. Summary

In conclusion, the dynamical origins of excess $\langle p_t \rangle$ fluctuations in Au–Au collisions at RHIC are studied in this analysis of two-particle correlations on (p_{t1}, p_{t2}) . The velocity/temperature structure of heavy ion collisions suggested by these correlations is unanticipated by theoretical models [9–11]. Lacking in these models is the simultaneous inclusion of hard scattering in the initial state with subsequent medium modification of the fragmentation function and/or interactions between the medium and the hadrons associated with the scattered partons. Nevertheless it seems plausible to interpret the observed correlations on (p_{t1}, p_{t2}) as resulting from this sort of semi-hard parton scattering and subsequent medium modified fragmentation and/or associated hadron distributions on p_t in the more central Au–Au collisions. In this picture, with increasing centrality the transverse momentum associated with the two-particle fragment distribution from initial-state semi-hard parton scattering is shifted to lower p_t , asymptotically approaching a form consistent with random velocity/temperature variations (Lévy saddle) as a manifestation of substantial but incomplete equilibration. These newly-observed p_t correlations may thus reveal minijet dissipation in the medium produced by Au–Au collisions at RHIC.

Acknowledgments

We thank the RHIC Operations Group and RCF at BNL, and the NERSC Center at LBNL for their support. This work was supported in part by the Offices of NP and HEP within the US DOE Office of Science; the US NSF; the BMBF of Germany; IN2P3, RA, RPL, and EMN of France; EPSRC of the United Kingdom; FAPESP of Brazil; the Russian Ministry of Science and Technology; the Ministry of Education and the NNSFC of China; IRP and GA of the Czech Republic, FOM of the Netherlands, DAE, DST and CSIR of the Government of India; Swiss NSF; the Polish State Committee for Scientific Research; SRDA of Slovakia and the Korea Sci. & Eng. Foundation.

References

- [1] Stock R 1999 *Nucl. Phys. A* **661** 282c
Heiselberg H 2001 *Phys. Rep.* **351** 161
- [2] Dumitru A and Pisarski R 2001 *Phys. Lett. B* **504** 282
- [3] Stephanov M, Rajagopal K and Shuryak E 1999 *Phys. Rev. D* **60** 114028
- [4] Adler C *et al* 2003 *Phys. Rev. Lett.* **90** 082302
- [5] Adler S S *et al* (PHENIX Collaboration) 2006 *Phys. Rev. Lett.* **97** 052301
- [6] Adams J *et al* (STAR Collaboration) 2005 *Phys. Rev. C* **71** 064906
- [7] Adler S S *et al* (PHENIX Collaboration) 2004 *Phys. Rev. Lett.* **93** 092301
- [8] Appelshäuser H *et al* (NA49 Collaboration) 1999 *Phys. Lett. B* **459** 679
Adamová D *et al* (CERES Collaboration) 2003 *Nucl. Phys. A* **727** 97
- [9] Wang X-N and Gyulassy M 1991 *Phys. Rev. D* **44** 3501
- [10] Sorge H, Stöcker H and Greiner W 1989 *Nucl. Phys. A* **498** 567c
Sorge H, Stöcker H and Greiner W 1989 *Ann. Phys. (N.Y.)* **192** 266
- [11] Lin Z-W, Ko C M, Li B-A, Zhang B and Pal S 2005 *Phys. Rev. C* **72** 064901

- [12] Adler C *et al* 2002 *Phys. Rev. C* **66** 034904
- [13] Adler C *et al* (STAR Collaboration) 2001 *Phys. Rev. Lett.* **87** 082301
- [14] Andersson B, Gustafson G, Ingelman G and Sjöstrand T 1983 *Phys. Rep.* **97** 31
- [15] Gaździcki M, Leonidov A and Roland G 1999 *Eur. Phys. J. C* **6** 365
- [16] Liu Q and Trainor T A 2003 *Phys. Lett. B* **567** 184
- [17] Ackermann K H *et al* 2003 *Nucl. Instrum. Methods A* **499** 624 (see other STAR papers in this volume)
- [18] Related to but not equivalent to the power-law exponent in Adler C *et al* (STAR Collaboration) 2001 *Phys. Rev. Lett.* **87** 112303
Adler C *et al* (STAR Collaboration) 2002 *Phys. Rev. Lett.* **89** 202301
- [19] Ishihara A 2004 *PhD Thesis* The University of Texas at Austin, unpublished
- [20] Adams J *et al* (STAR Collaboration) 2006 *Phys. Rev. C* **73** 064907
- [21] Adams J *et al* (STAR Collaboration) 2006 *Phys. Lett. B* **634** 347
- [22] Whitmore J 1976 *Phys. Rep.* **27** 187
Kafka T *et al* 1977 *Phys. Rev. D* **16** 1261
- [23] Porter R J and Trainor T A (STAR Collaboration) 2005 *J. Phys. Conf. Ser.* **27** 98
- [24] Trainor T A 2000 *Preprint hep-ph/0001148*; the summation in equation (2) includes factor N_j/\bar{N} relative to that in [6]
- [25] Condon E U and Odishaw H 1967 *Handbook of Physics 2nd edn*, ed C Eisenhart and M Zelen (New York: McGraw-Hill) chapter 12, pp 1–177, 178
- [26] Ray R and Longacre R 2000 *Preprint nucl-ex/0008009*
- [27] Reid J G 2003 *PhD Thesis* University of Washington *Preprint nucl-ex/0302001*
- [28] Anticic T *et al* (NA49 Collaboration) 2004 *Phys. Rev. C* **70** 034902
- [29] Hwa R and Yang C 2002 *Phys. Rev. C* **66** 025205
Chiu C B and Hwa R C 2006 *Phys. Rev. C* **73** 014903
- [30] Schnedermann E, Sollfrank J and Heinz U 1993 *Phys. Rev. C* **48** 2462
Tomášik B and Heinz U 2002 *Phys. Rev. C* **65** 031902 (R)
- [31] Tannenbaum M J 2001 *Phys. Lett. B* **498** 29
- [32] Wilk G and Włodarczyk Z 2000 *Phys. Rev. Lett.* **84** 2770 (similar to a ‘power-law’ distribution [18])
- [33] Porter R J and Trainor T A (STAR Collaboration) 2004 *Preprint hep-ph/0406330*
- [34] Wang X-N 1992 *Phys. Rev. D* **46** R1900
Wang X-N and Gyulassy M 1992 *Phys. Lett. B* **282** 466
- [35] Adams J *et al* 2003 *Phys. Rev. Lett.* **91** 172302
- [36] Adcox K *et al* 2002 *Phys. Rev. Lett.* **88** 022301
Back B B *et al* 2005 *Phys. Rev. Lett.* **94** 082304
Arsene I *et al* 2003 *Phys. Rev. Lett.* **91** 072305